Three-dimensional modeling of amplitude-object imaging in scanning near-field optical microscopy

Elena Vasilyeva and Allen Taflove

Department of Electrical and Computer Engineering, Northwestern University, Evanston, Illinois 60208-3118

Received March 26, 1998

The imaging properties of the transmission-illumination mode of a scanning near-field optical microscope are investigated. Three-dimensional calculations of the power transmitted into classically allowed and forbidden regions for a nonsymmetrically positioned amplitude object are implemented by use of the finite-difference time-domain solution of Maxwell's equations. The evolution of the images with the distance from the object as well as the effect of the polarization of the illumination is shown. The computations show that for applications involving the imaging of an amplitude object, the use of the allowed light is preferred. Collection of light from both the allowed and the forbidden zones leads to degraded contrast and resolution. © 1998 Optical Society of America

OCIS codes: 180.5810, 240.7040.

One generates optical images in the transmission mode of a scanning near-field optical microscope (SNOM) by scanning an optical probe over the sample and recording the transmitted signal as a function of the probe position. The tunnel scanning near-field optical microscope detects not only the regularly transmitted waves but also the radiation coupled by evanescent waves to the classically forbidden directions (angles larger than the angle of total internal reflection). Forbidden light can, in some cases, provide images with contrast and resolution higher than those of the standard SNOM in the allowed light. However, the contrast of the scan images depends on the dielectric properties of the object. It was shown experimentally that phase-object images have positive contrast in allowed light and negative contrast in forbidden light, whereas amplitude-object images have negative contrast in both types of light.[1] Different contrast mechanisms were also investigated analytically by use of a single dipole located above a planar dielectric substrate as a light source.[2] In numerical studies of SNOM the multiple-multipole method[3–5] was shown to be useful for two-dimensional (2-D) modeling. However, this method may be less suitable for three-dimensional (3-D) simulations owing to difficulties in dealing with complicated inhomogenous material geometries. Another approach based on an iterative Green function method was also proposed.[6,7]

The finite-difference time-domain (FDTD) method[8] may present a better alternative for 3-D SNOM modeling because it permits an arbitrary material permittivity and permeability to be specified at each electric- and magnetic-field component location. The FDTD method solves for the electromagnetic field in time and space with the full-wave coupled Maxwell's curl equations. Centered finite-difference expressions are used for the space and time derivatives. FDTD was used for 2-D simulations of the field patterns in illumination SNOM[9] and for 3-D simulations of image formation in collection-type SNOM.[10]

The present study involves a FDTD-based numerical investigation of the near-field optical imaging mechanism of the tunnel SNOM by use of a realistic 3-D configuration. This configuration involves a nonsymmetrical positioning of a metal scattering object relative to a conical metal-clad glass taper. We note that this configuration could not be modeled by rotationally symmetric formulations.[11]

We compute the images of an amplitude object in the transmission-illumination mode. Figure 1 shows the FDTD geometry of the model under investigation for two cases. For case 1 the total (x, y, z) size of the model is 400 nm × 400 nm × 400 nm (100 × 100 × 100 cells); for case 2 the model size is 400 nm × 400 nm × 480 nm (100 × 100 × 120 cells). In each case the absorbing boundary condition used at the outer planes of the space lattice is Berenger's perfectly matched layer,[12] which yields a reflection coefficient of the order of 0.0001 for the parameters used in this model. For the purposes of our simulation the outer boundary is effectively transparent.

A TE_{11} mode excites a conical metal-clad glass taper having an aperture diameter of 24 nm (6 cells). The glass taper illuminates a metal object of size 64 nm × 64 nm × 16 nm (16 × 16 × 4 cells) with light of wavelength $\lambda = 488$ nm. We conduct multiple FDTD runs to obtain the image. For each simulation the metal object is positioned at a specific location along the x direction on the surface of a glass substrate of refractive

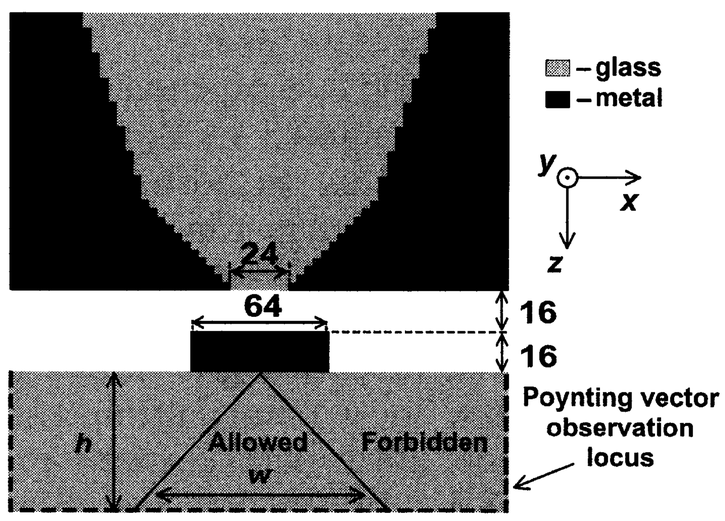

Fig. 1. FDTD geometry of the TNOM model. All dimensions are in nanometers.

0146-9592/98/151155-03$15.00/0

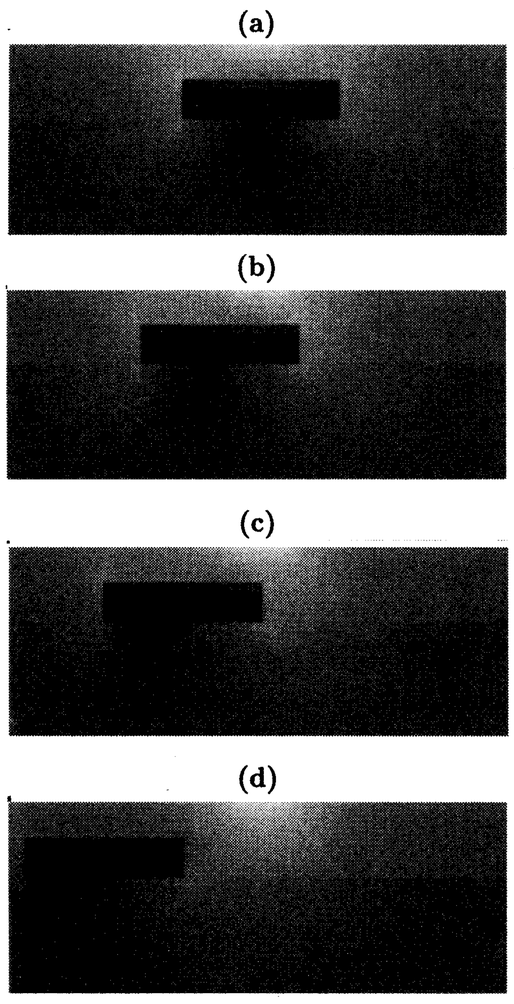

Fig. 2. FDTD-computed TNOM electric-field distribution as a function of the object distance from the axis of the glass taper: (a) 0 nm, (b) 16 nm, (c) 32 nm, (d) 64 nm. The dynamic range is saturated to render weak intensity values visible.

index $n = 1.47$. In our model s and p polarizations are excited by the y- and x-polarized components of the TE_{11} mode, respectively. The Poynting vector is calculated in the output z plane located in the glass substrate h nm below the surface, and in the x- and y-plane boundaries of the substrate (Fig. 1, dashed lines). At the output z plane the width of the allowed region is w nm, as determined by the angle of total internal reflection. The transmitted power is found by integration of the appropriate normal component of the Poynting vector. At each probe position the calculated transmitted power is normalized to the total transmitted power observed with no object present.

Figure 2 shows gray-scale visualizations of the magnitude squared of the FDTD-computed electric field at various object distances from the axis of the glass taper. The lattice size of case 1 is used. Here the light is polarized in the direction of the scan. It can be seen that there is a distinct shadow region formed by the object despite its small electrical size. Further, there is clearly a field enhancement at the sides of the object. The shadow-region intensity profile leads to a negative-contrast image of the object.

Figure 3 shows the FDTD-computed scan images generated with the probe shown in Fig. 1 in allowed and forbidden light as well as for both s and p polarizations. The lattice size of case 1 is used; $h = 80$ nm (20 cells) and $w = 148$ nm (37 cells). Both allowed- and forbidden-light scan images show negative contrast. In Fig. 3(a), the allowed-light image is 72 nm wide at half-maximum in p polarization and 84 nm wide in s polarization. Both polarizations exhibit an image contrast of 13.8:1. In Fig. 3(b) the object image in the forbidden light is 87 nm wide at half-maximum for both polarizations and exhibits a contrast of 4.0:1.

Figure 4 shows the FDTD-computed images obtained for the lattice size of case 2. Here $h = 200$ nm (50 cells) and $w = 372$ nm (93 cells). In Fig. 4(a) the allowed-light image is 59 nm wide at half-maximum in p polarization and 67 nm wide in s polarization. Both polarizations exhibit an image contrast of 9.4:1. In Fig. 4(b) the forbidden-light images are distorted and show strong dependence on the polarization of the illuminating light.

Our calculations to date are limited to distances of 200 nm from the object (approximately three times the object size). At this distance the forbidden light may not yet be completely separated from the allowed light. Indeed, complete separation takes place at distances at which the size of the allowed region is much larger than that of the object; this is only approximately true in our model, in which the allowed region is 5.8 times larger than the object. However, the major image trends are already apparent. That is, the allowed light image exhibits negative contrast of a higher value

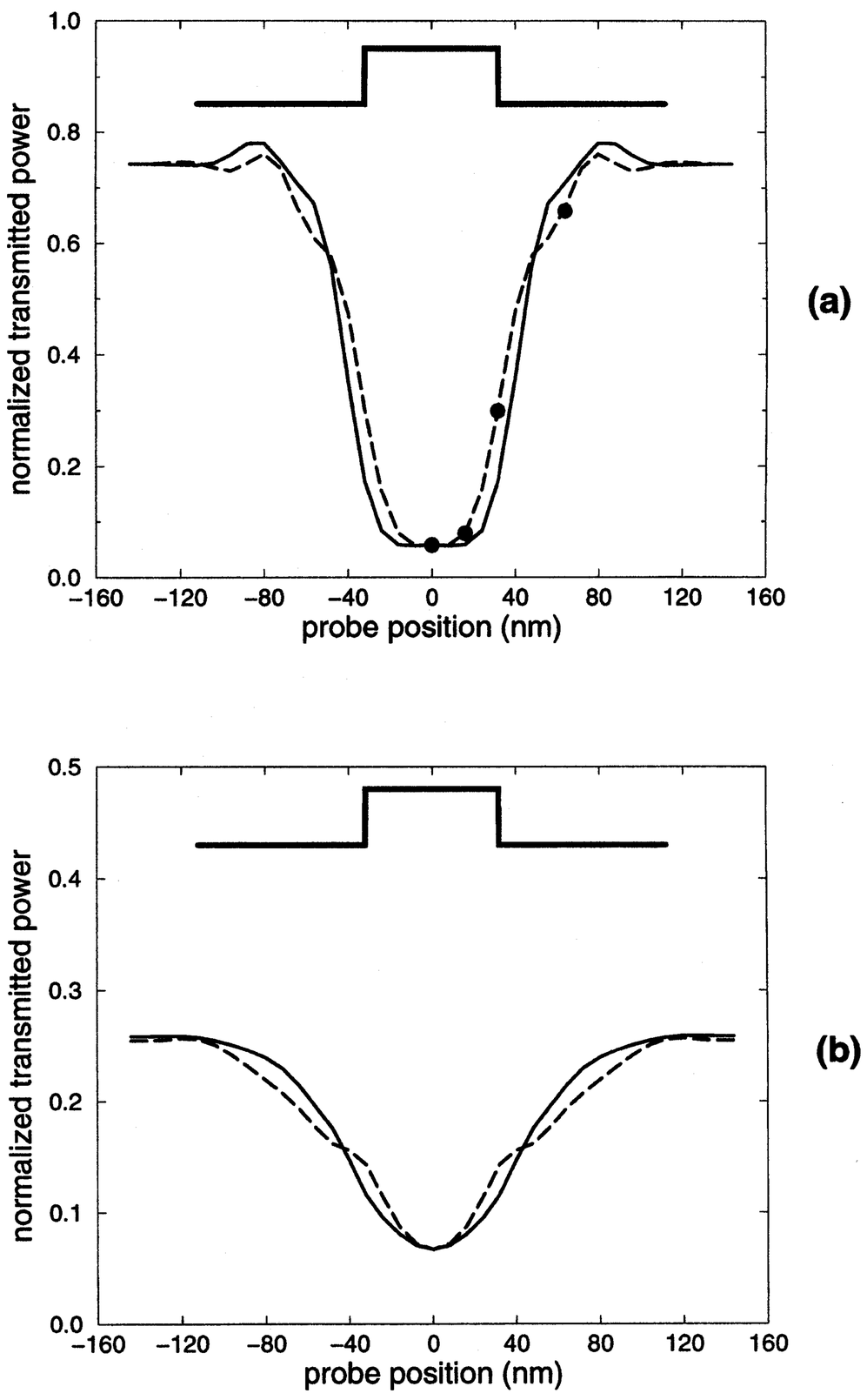

Fig. 3. FDTD-computed TNOM images generated at an observation locus 80 nm below the object in (a) allowed light and (b) forbidden light. Dashed curves, p polarization; solid curves, s polarization; thick solid lines, geometric profiles of the 64-nm-wide sample; filled circles, locations of the corresponding visualizations in Fig. 2.

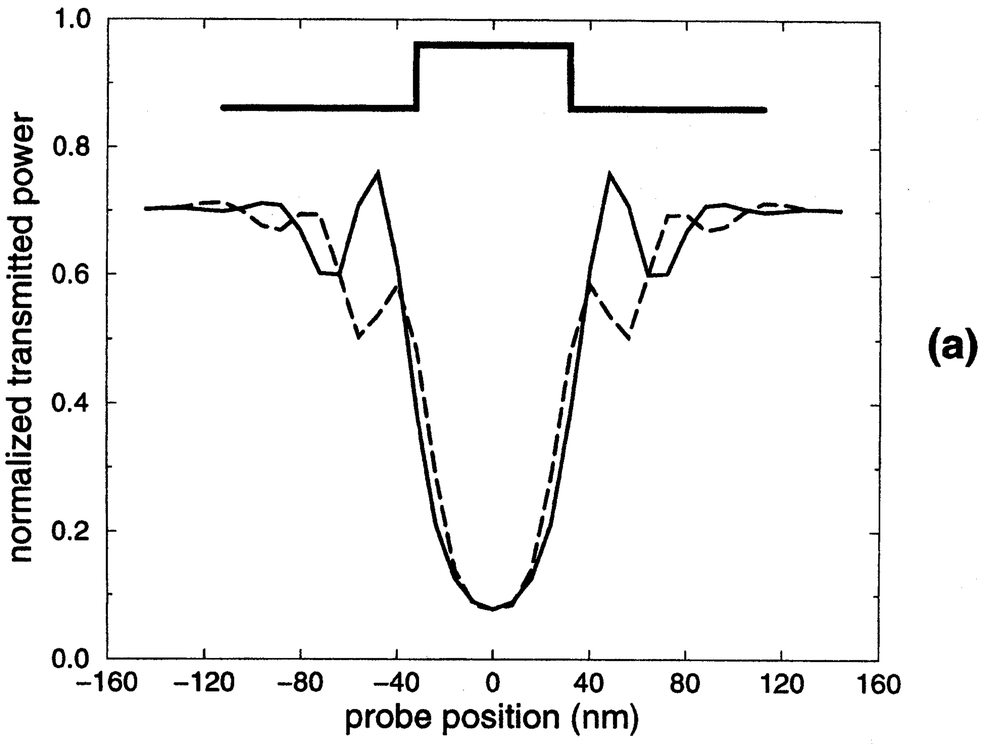

Fig. 4. FDTD-computed TNOM images generated at an observation locus 200 nm below the object in (a) allowed light and (b) forbidden light. The curves (lines) are the same as in Fig. 3.

than that of the forbidden light and little dependence on the polarization of the illumination. Further, the forbidden-light image is distorted and exhibits strong polarization dependence. For applications involving the imaging of an amplitude object, the use of the allowed light is preferred. Collection of light from both the allowed and the forbidden zones leads to degraded contrast and resolution.

We thank M. Aamodt and his colleagues at Cray Research, Inc., for providing the supercomputing resources used for this study.

References

1. B. Hecht, D. W. Pohl, H. Heinzelmann, and L. Novotny, Ultramicroscopy **61,** 99 (1995).
2. L. Novotny, J. Opt. Soc. Am. A **14,** 91 (1997).
3. L. Novotny, D. W. Pohl, and P. Regli, J. Opt. Soc. Am. A **11,** 1768 (1994).
4. L. Novotny, D. W. Pohl, and B. Hecht, Ultramicroscopy **61,** 1 (1995).
5. D. W. Pohl, L. Novotny, B. Hecht, and H. Heinzelmann, Thin Solid Films **273,** 161 (1996).
6. O. J. F. Martin, A. Dereux, and C. Girard, J. Opt. Soc. Am. A **11,** 1073 (1994).
7. O. J. F. Martin, C. Girard, and A. Dereux, Phys. Rev. Lett. **74,** 526 (1995).
8. A. Taflove, *Computational Electrodynamics: The Finite-Difference Time-Domain Method* (Artech House, Norwood, Mass., 1995).
9. D. A. Christensen, Ultramicroscopy **57,** 189 (1993).
10. H. Furukawa and S. Kawata, Opt. Commun. **132,** 170 (1996).
11. A. J. Ward and J. B. Pendry, J. Mod. Opt. **44,** 1703 (1997).
12. J.-P. Berenger, J. Comput. Phys. **114,** 185 (1994).